DOI 10.1007/s10946-024-10194-6
Journal of Russian Laser Research, Volume 45, Number 1, January, 2024

CORROSION PERFORMANCE OF GRAPHENE-STRENGTHENED $CoCrFeNiMo_{0.2}$ HIGH-ENTROPY ALLOY IN SIMULATED ACID RAIN PREPARED BY LASER CLADDING

Xingwu Qiu

Multicomponent Alloys Key Laboratory of Deyang City
Sichuan College of Architectural Technology
Deyang 618000, China

Department of Materials Engineering
Sichuan College of Architectural Technology
Deyang 618000, China

E-mail: qiuxingwu2021@163.com

Abstract

We study the graphene (Gr)-strengthened $CoCrFeNiMo_{0.2}$ high-entropy alloys (HEAs) prepared by laser cladding. The corrosion properties of the alloys under simulated acid rain conditions are studied through rainfall experiments, electrochemical experiments, and immersion experiments. The experimental results show that the microstructure of the Gr-strengthened $CoCrFeNiMo_{0.2}$ HEAs mainly including three morphologies. Mo element occurs segregation. Gr concentrates on the alloy surface during melting. The alloy has a face centered cubic (FCC) single-phase structure. With increase in the rainfall and immersion period, the corrosion resistance of the Gr-strengthened HEAs decreases. With increase in the pH, the corrosion resistance of the alloys increase. The corrosion current densities of Gr-strengthened $CoCrFeNiMo_{0.2}$ HEAs are small, indicating that the alloys have excellent corrosion resistance. Electrochemical impedance spectroscopy (EIS) shows that as the pH increases, the capacitance arc radius, impedance modulus, and phase angle show increasing trend. The reason for excellent corrosion resistance are as follows: the Gr enriched on the surface plays a shielding role during alloy melting, Gr reacts with alloy elements to form a passive film on the alloy surface, the lattice distortion and grain refinement are caused by Gr, providing the single-phase structure of the alloy.

Keywords: graphene, high-entropy alloy coating, simulated acid rain, microstructure, laser cladding, corrosion performance.

1. Introduction

The impact of human activities on the environment is becoming increasingly prominent. Burning fossil fuels such as coal, oil, and natural gas with high Sulfur content cause acidification of rainfall, and acid rain is formed when $pH < 5.6$ [1]. In metals exposed to the atmosphere corrode under the influence of the environment, the acidification of rainwater significantly accelerates the corrosion rate of metals [2,3]. Traditional research on the corrosion behavior of metals in acid rain usually uses the outdoor hanging method [4], which processes the metal into a specified size and hangs it outdoors. By collecting data, the corrosion situation of metals under acid rain conditions is calculated and compared with the

Manuscript submitted by the author in English on December 25, 2023.

corrosion situation of metals in ordinary rainwater environments. Although this method is intuitive, the disadvantage is that it requires a long time for materials to complete the experiment and wastes manpower. Therefore, in this article, we study the composition of acid rain and manually simulates acid rain, using chemicals to prepare acidic rainwater.

Ordinary metals have a high corrosion rate in acid rain environments, but the working environment of some devices (such as rain gauges) determines that they must be exposed to the natural environment. Therefore, it will directly affect its service life. In order to improve its corrosion resistance in acid rain, it is necessary to strictly select its constituent materials. HEAs is a new type of metal material [5–12]. Its excellent properties [13–24] have attracted extensive attention of experts and scholars in recent years [25–33]. In this study, we prepare HEAs strengthened by Gr, with the aim of exhibiting excellent corrosion resistance in acid rain environments.

2. Experimental

We select Co, Cr, Fe, Ni, Mo metal powders with element purity $>99.9\%$ as cladding materials and use Gr as the reinforcement material with a content of 0.40 wt.%. The mixed powder is ball milled in a planetary mill for 4 h. at a rotating speed of 300 r/min. 40 Cr steel is used as a substrate, where the powder is grounded, and oil stains are removed from the surface to ensure cleanliness. Then, we utilize a complete set of CO_2 laser cladding equipment (LSJG-GQ-6000) for laser cladding treatment, use powder presetting method, place the mixed powder on the surface of the substrate in advance, and perform laser scanning. The laser processing parameters are as follows: the laser power $P = 2500$ W, the scanning speed $V = 5$ mm/s, and the laser spot diameter $D = 3.5$ mm.

We analyze the composition of natural acid rain in Sichuan province, China and prepare simulated acid rain solution, as shown in Table 1. Using standard sulfuric acid solution, we regulate the pH of simulated acid rain solution.

Table 1. Composition of Simulated Acid Rain [mg/L].

Mg^{2+}	Na^{+}	SO_4^{2-}	NH_4^{+}	K^{+}	NO_3^{-}	F^{-}	Ca^{2+}
2.64	7.25	13.83	4.21	2.18	5.16	1.36	7.63

We use scanning electron microscope (KYKY-EM3200) to analyze the microstructure of the Gr-strengthened $CoCrFeNiMo_{0.2}$ HEAs and its attached energy spectrometer to analyze the micro-area composition. X-ray diffraction (DX-2600) is used to analyze the crystal structure of the alloy. The test conditions are: Cu target, radiation at 40 kV and 25 mA, the scanning ranges from 20° to 100°, with a scan speed of 4°/min. The corrosion performance of alloys in simulated acid rain environments with pH = 3.8, 4.3, 4.8, and 5.3 is tested by simulated rainfall equipment (KLD-IP1.2-400). The equipment can adjust the rain intensity, raindrop size, and rainfall time. During testing, the samples are placed on the sample table in the rainfall chamber, the sample table speed is adjusted to truly simulate natural rainfall conditions; in the experiment, the rainfall time for each cycle is set to 30 min. After being exposed to rain, we take the samples out of the rainfall chamber and dry them; also, we measure the mass of the samples before and after each cycle. Then, the samples are placed in the rainfall chamber again for 30 min. of rainfall. This is repeated, and the samples are tested for 10 cycles in simulated acid rain solutions of each pH condition. The electrochemical corrosion performance of Gr-strengthened $CoCrFeNiMo_{0.2}$ HEAs in simulated acid rain environments with pH = 3.8, 4.3, 4.8, and 5.3 are tested, using electrochemical workstation (CS310M). The polarization curves, cyclic polarization curves, and EIS of the alloys are measured. The comprehensive corrosion behavior of the alloys in simulated acid rain

environments with pH = 3.8, 4.3, 4.8, and 5.3 are tested, using the immersion method. The immersion time is once every 24 h., and the sample mass is measured before and after immersion, a total of 10 cycles are tested under each pH condition.

3. Results and Discussion

3.1. Microstructure and XRD

In Fig. 1, we illustrate the microstructure of Gr-strengthened $CoCrFeNiMo_{0.2}$ HEAs, where three morphologies marked as *A*, *B* and *C*, respectively, are shown. The formation of alloy structure is closely related to the content of each element and melting point, as well as the cooling rate during laser cladding. Element area scanning is performed on the microstructure in Fig. 1 a, b, and the results are shown in

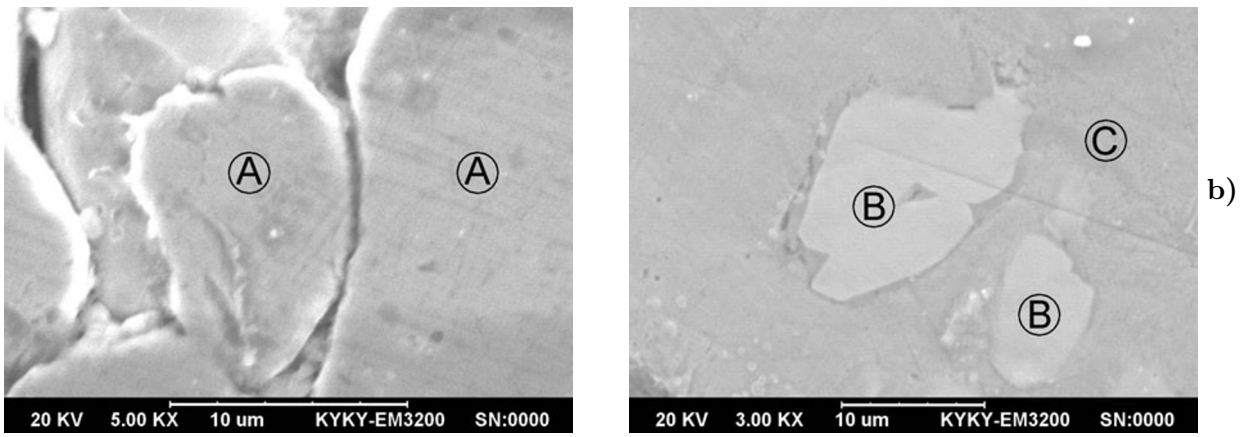

Fig. 1. Microstructure of Gr-strengthened $CoCrFeNiMo_{0.2}$ HEAs.

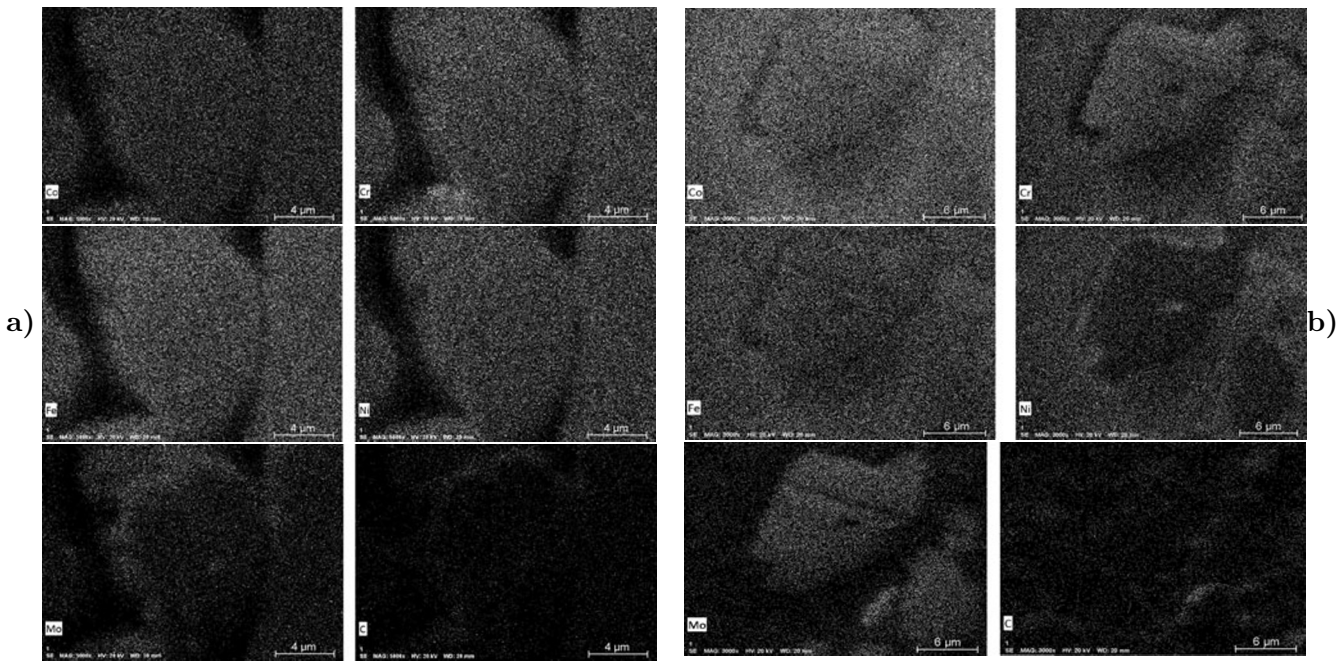

Fig. 2. EDS mapping of Gr-strengthened $CoCrFeNiMo_{0.2}$ HEA.

Fig. 2 a b. The Mo element exhibits uneven distribution, which is mainly distributed in the grains of A and B, this is related to its mixing enthalpy between Mo and other elements.

In Fig. 3, we present the X-ray diffraction pattern of Gr-strengthened $CoCrFeNiMo_{0.2}$ HEA. From the analysis, one can see that the alloy phase has a simple FCC structure. The alloy has five elements and six elements after the addition of Gr-strengthened phase. The multi-element effect inhibits the emergence of complex intermetallic compounds, making the alloy to show a single FCC structure.

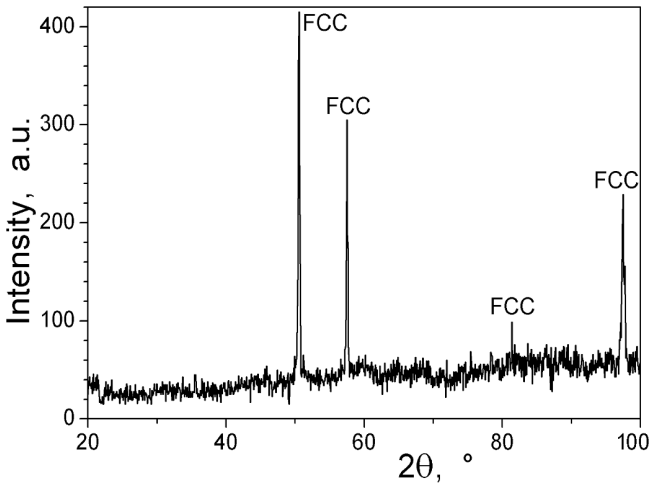

Fig. 3. XRD pattern of Gr-strengthened $CoCrFeNiMo_{0.2}$ HEA.

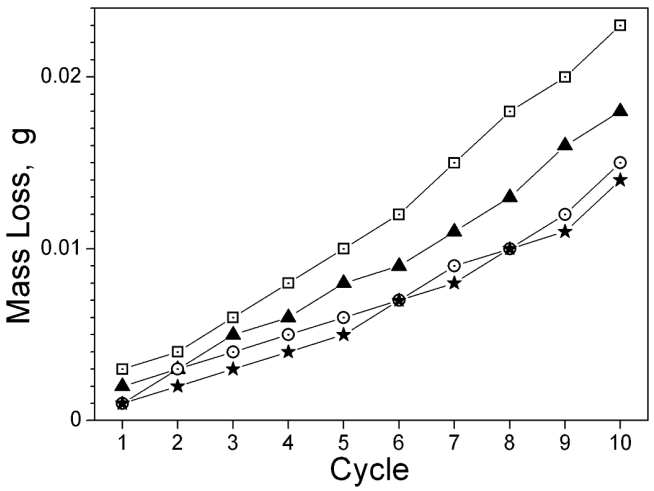

Fig. 4. Mass loss of Gr-strengthened $CoCrFeNiMo_{0.2}$ HEAs in rainfall experiments. Here, pH = 3.8 (⊡), pH = 4.3 (▲), pH = 4.8 (⊙), and pH = 5.3 (⋆).

3.2. Corrosion Behavior

In Fig. 4, we show the mass loss results of Gr-strengthened HEAs after simulated acid rain rainfall experiments.

After 10 cycles rainfall experiments, the mass loss is very small, indicating excellent corrosion resistance. Due to the low melting point, the Gr is easy to float on the alloy surface during melting, which is beneficial to the corrosion resistance of the alloy surface. The two-dimensional lamellar structure of Gr is easy to stack, forming a dense physical insulation layer. It is difficult for corrosive medium to pass through the dense insulating layer, and Gr, as a good shielding agent, insulates the metal matrix from the surrounding environment. In addition, the surface effect of Gr makes the contact angle between Gr and corrosive liquid very large, which makes it difficult for liquid molecules to spread on the surface of Gr, thus, playing the role of anti-corrosion.

Table 2. Corrosion Dynamics Parameters of Gr-Strengthened $CoCrFeNiMo_{0.2}$ HEAs in Simulated Acid Rain Solutions.

pH	E_{corr}, V	I_{corr}, A$\cdot$ cm^{-2}
3.8	−0.40	$2.5 \cdot 10^{-3}$
4.3	−0.58	$6.8 \cdot 10^{-4}$
4.8	−0.56	$6.7 \cdot 10^{-4}$
5.3	−0.46	$6.5 \cdot 10^{-4}$

As the rainfall cycle increases, the mass loss of the alloys under different pH conditions shows an increasing trend, which is due to the exacerbation of corrosion degree with increase in the cycle. As the pH increases, the mass loss of the alloy shows a decreasing trend under the same cycle conditions. This is because the higher the pH, the lower the H^+ concentration, and the lower the degree of corrosion.

In Fig. 5, we display the polarization curves of Gr-strengthened $CoCrFeNiMo_{0.2}$ HEAs in simulated acid rain solution with different pH conditions. In Table 2, we show the corrosion kinetics parameters obtained through linear fitting. The low corrosion current density of the alloys in simulated acid rain indicates excellent corrosion resistance.

As the pH increases, the corrosion current density shows a decreasing trend, indicating an enhanced corrosion resistance. The excellent corrosion resistance is due to the following factors: first, the formation of a passivation film on the surface of the alloy, which protects the internal alloy and effectively prevents the immersion of H^+. Second, both Mo element and Gr-strengthening phase in the alloys play a role in refining grains, reducing intergranular corrosion and improving the overall corrosion resistance of the alloy. Third, the alloy's

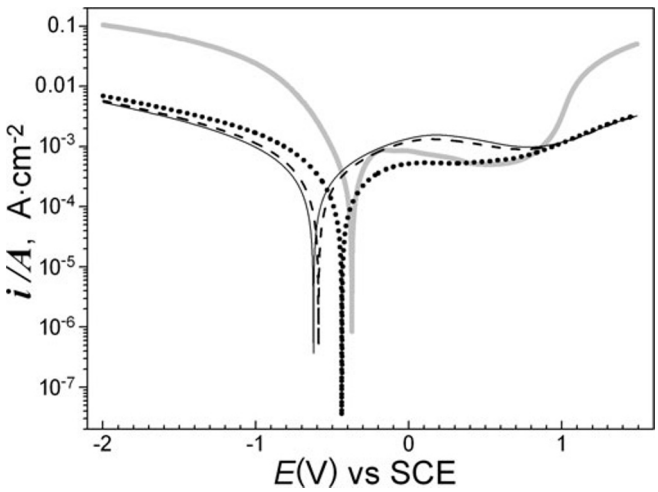

Fig. 5. Polarization curves of Gr-strengthened $CoCrFeNiMo_{0.2}$ HEAs in simulated acid rain solutions with pH = 3.8 (the gray curve), pH = 4.3 (the solid curve), pH = 4.8 (the dashed curve), and pH = 5.3 (the dotted curve).

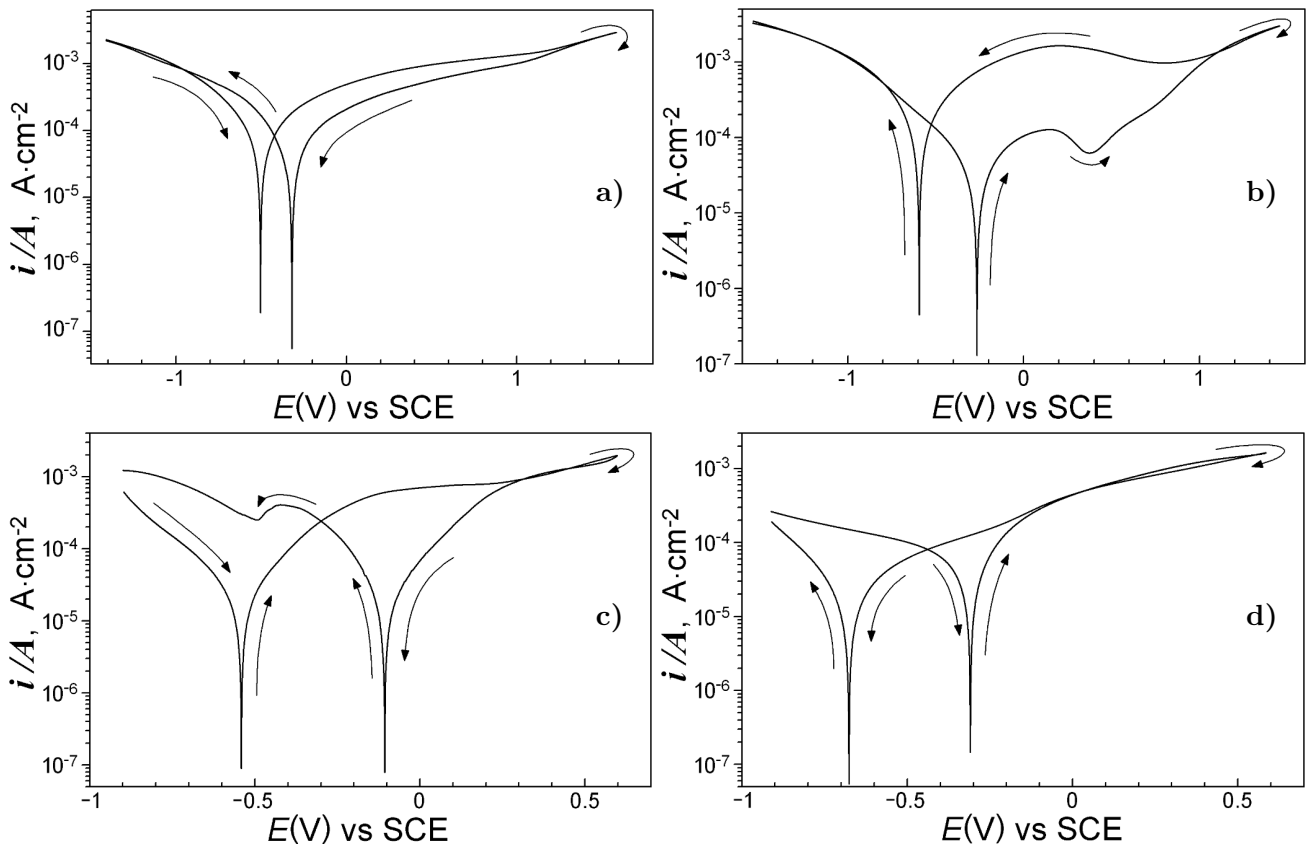

Fig. 6. Circular polarization curves of Gr-strengthened $CoCrFeNiMo_{0.2}$ HEAs in simulated acid rain solutions when pH = 3.8 (a), 4.3 (b), 4.8 (c), and 5.3 (d).

structure is a single FCC structure, reducing the impact of the formation of micro-corrosive batteries [34]. Fourth, the addition of Gr aggravates the lattice distortion, making the immersion of H^+ more difficult.

In order to characterize the pitting corrosion resistance of Gr-strengthened $CoCrFeNiMo_{0.2}$ HEAs, we test the cyclic polarization curves of the alloys in simulated acid rain solutions with different pH; the test results are shown in Fig. 6.

We find that there is basically no hysteresis loop on the cyclic polarization curve, when pH = 3.8. As pH increases, hysteresis loop gradually appears on the cyclic polarization curves. When pH = 4.3, it is shown that a negative hysteresis loop appears. When pH increases to 4.8, a negative hysteresis loop appears, and when pH = 5.3, the area of the hysteresis loop is larger. The above situation indicates that the alloys does not exhibit pitting corrosion when the pH > 3.8.

In order to study the corrosion resistance of the alloy surface during electrochemical corrosion, we test the EIS of Gr-strengthened $CoCrFeNiMo_{0.2}$ HEAs in simulated acid rain solutions with different pH. In Fig. 7, we show the test results, including the Nyquist plot, $|Z|$-frequency plots and phase angle–frequency plots. A relatively regular capacitive reactance arc can be seen in the high-frequency area of the Nyquist plot, indicating that the corrosion process is controlled by the charge transfer process [35,36]. The size of the capacitive arc radius corresponds to the size of the impedance. The corrosion resistance of different pH is compared by the radius of the capacitive arc. The larger the radius, the better the corrosion resistance of the alloy [37].

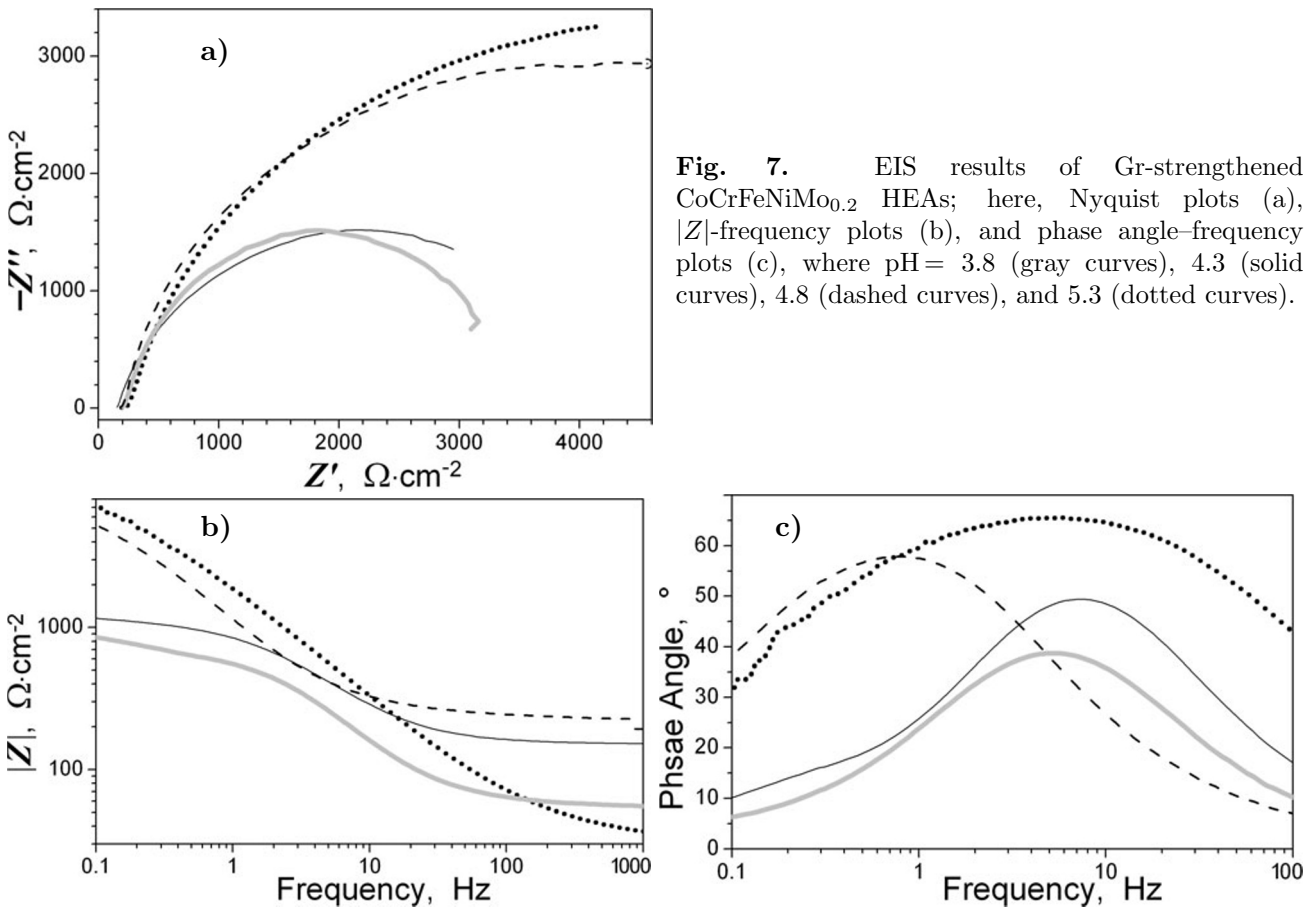

Fig. 7. EIS results of Gr-strengthened $CoCrFeNiMo_{0.2}$ HEAs; here, Nyquist plots (a), $|Z|$-frequency plots (b), and phase angle–frequency plots (c), where pH = 3.8 (gray curves), 4.3 (solid curves), 4.8 (dashed curves), and 5.3 (dotted curves).

In Fig. 7 a, we see that with increase in the pH, the radius of the capacitive arc tends to increase. In Fig. 7 b, we see that the impedance modulus increases with increase in the pH and reaches its maximum when pH = 5.3. In phase angle–frequency plots, we realize that with increase in the pH, the phase angle shows an increasing trend, with the maximum phase angle ranging from 65° to 70°. The larger the phase angle, the better the corrosion resistance of the alloy. Based on Fig. 7, we conclude that $CoCrFeNiMo_{0.2}$ HEAs exhibit the highest impedance modulus and phase angle when pH = 5.3, demonstrating the best corrosion resistance.

The mass loss results of Gr-strengthened $CoCrFeNiMo_{0.2}$ HEAs in simulated acid rain immersion test are listed in Fig. 8.

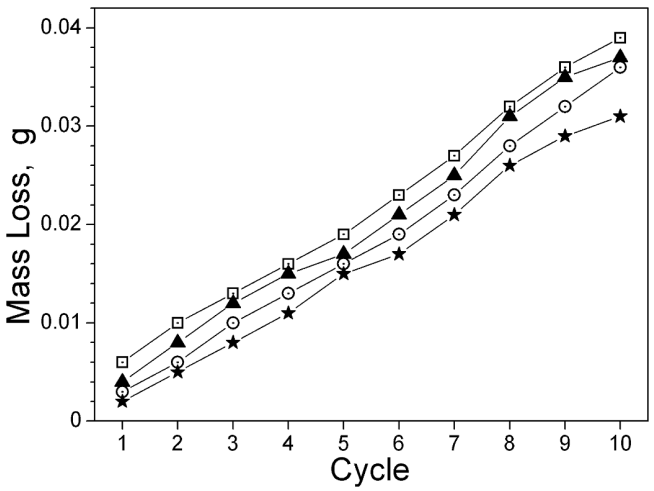

Fig. 8. Mass loss of Gr-strengthened $CoCrFeNiMo_{0.2}$ HEAs in simulated acid rain immersion experiments. Here, pH = 3.8 (⊡), 4.3 (▲), 4.8 (⊙), and 5.3 (⋆).

With increase in the immersion period, the mass loss of the alloys under different pH conditions shows an increasing trend, this is because increase in the cycle intensifies the corrosion degree. As the pH increases, the mass loss of the alloy shows a decreasing trend under the same cycle conditions. This is because the higher the pH, the lower the H^+ concentration, and the lower the degree of corrosion. Gr with smaller particle size is filled into the alloy's micro-holes and defects, which extend the diffusion path of the corrosion medium to a certain extent, thus, preventing and delaying the corrosion medium from immersing solution into the alloy interior, and enhancing the corrosion resistance. At the same time, Gr reacts with alloy elements, resulting in passivation or formation of protective film on the alloy surface, enhancing the protective ability of the alloy, and further improving its corrosion resistance.

In Fig. 9 a, we present the surface corrosion morphology of Gr-strengthened $CoCrFeNiMo_{0.2}$ HEAs after simulated acid rain rainfall experiment with pH = 3.8. In Fig. 9 b, the element area scanning result is presented. Under the action of H^+, the passivation film of the alloy is damaged, H^+ immerses into the interior of the alloy at the location, where the passivation film is damaged, causing corrosion.

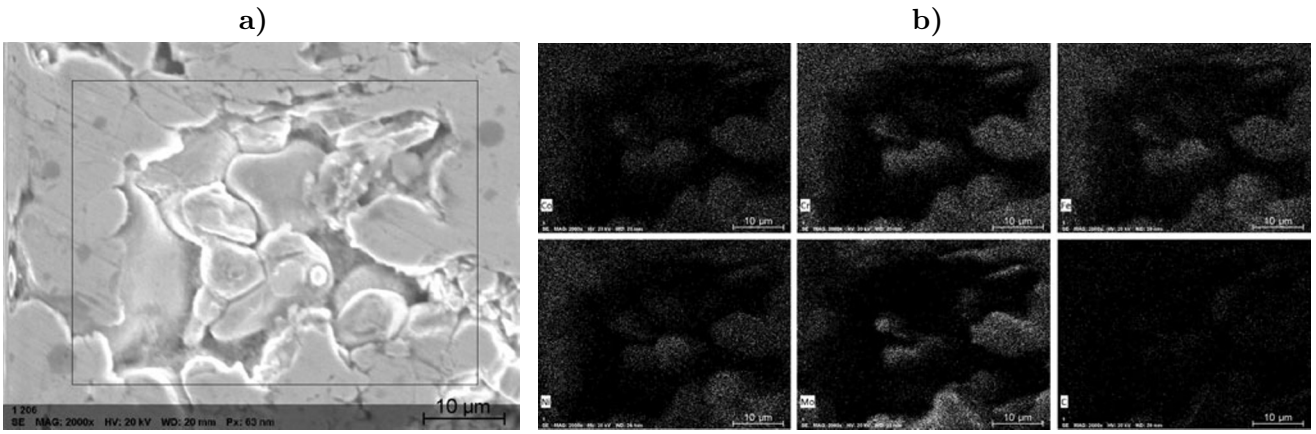

Fig. 9. Surface corrosion morphology and EDS mapping of Gr-strengthened $CoCrFeNiMo_{0.2}$ HEAs in simulated acid rain solutions with pH = 3.8.

4. Conclusions

To conclude, we point out

1. The microstructure of Gr-strengthened $CoCrFeNiMo_{0.2}$ HEAs mainly has three morphologies. Mo element occurs segregation, Gr concentrates on the alloy surface during melting. The alloy has a single-phase FCC structure.

2. With increase in the rainfall and immersion period, the corrosion resistance of the alloys decreases, while with increase in the pH, the corrosion resistance of the alloys increases. The Gr enriched on the alloy surface plays a shielding role, making the alloys to have excellent corrosion resistance.

3. The corrosion current density of Gr-strengthened $CoCrFeNiMo_{0.2}$ HEAs are small, indicating that the alloys have excellent corrosion resistance, which are related to the passive film formed on the alloy surface, fine grain, phase structure, and lattice distortion caused by Gr.

4. EIS shows that as the pH of the simulated acid rain increases, all the capacitance arc radius, impedance modulus, and phase angle show an increasing trend.

Acknowledgments

This work was supported by the Natural Science Foundation of Sichuan Province under Grant No. 2023NSFSC0406, Key R&D Guidance Projects in the Field of Social Development of Deyang City, Sichuan Province, China under Grant No. 2023SZZ138, and the Research Project of Sichuan College of Architectural Technology, Scientific Research and Innovation Team Foundation of Sichuan College of Architecture Technology under Grant No. SCJYKYCXTD 2022. We thank Dr. Xin Ren for editing English of this manuscript.

References

1. Y. M. Liu, W. T. Li, and Y. L. Zheng, *Acta Oecol.*, **120**, 103938 (2023); DOI: 10.1016/j.actao.2023.103938
2. M. Z. Chen, K. Yang, Z. D. Wang, et al., *Corros. Sci.*, **219**, 111232 (2023); DOI: 10.1016/j.corsci.2023.111232
3. C. B. Guo, Y. B. Lian, C. Huang, and Z. Y. Chen, *J. Mater. Res. Technol.*, **25**, 2306 (2023); DOI: 10.1016/j.jmrt.2023.05 283.
4. X. W. Qiu, C. G. Liu, J. Peng, and Z. S. Wang, *Kovove Mater.*, **61**, 59 (2023); DOI: 10.31577/km.2023.1.59
5. Z. Li, C. Jing, Y. Feng, et al., *Mater. Today Communicat.*, **35**, 105800 (2023); DOI: 10.1016/j.mtcomm.2023.105800
6. M. Zheng, C. Li, X. Zhang, et al., *Addit. Manufact.*, **37**, 101660 (2021); DOI: 10.1016/j.addma.2020.101660
7. Y. S. Lin, Y. C. Lu, and C. H. Hsueh, *Vacuum*, **211**, 111969 (2023); DOI: 10.1016/j.vacuum.2023.111969
8. X. W. Hong and C. H. Hsueh, *Intermetallics*, **140**, 107405 (2022); DOI: 10.1016/j.intermet.2021.107405
9. C. Liu, W. Lu, W. Xia, et al., *Nat. Commun.*, **13**, 1102 (2022); DOI: 10.1038/s41467-022-28706-w
10. T. Shun, L. Chang, and M. Shiu, *Mater. Charact.*, **70**, 63 (2012); DOI: 10.1016/j.matchar.2012.05.005
11. Z. F. He, N. Jia, H. W. Wang, et al., *J. Mater. Sci. Technol.*, **86**, 158 (2021); DOI: 10.1016/j.jmst.2020.12.079
12. A. Kumar, A. Singh, and A. Suhane, *J. Mater. Res. Technol.*, **17**, 2431 (2022); DOI: 10.1016/j.jmrt.2022.01.141
13. W. Y. Zhang, D. S. Yan, W. J. Lu, and Z. M. Li, *J. Alloy. Compd.*, **831**, 154799 (2020); DOI: 10.1016/j.jallcom.2020.154799
14. Y. L. Chou, Y. C. Wang, J. W. Yeh, and H. C. Shih, *Corros. Sci.*, **52**, 3481 (2010); DOI: 10.1016/j.corsci.2010.06.025

15. X. W. Liu, L. Liu, G. Liu, et al., *Met. Mater. Trans. A*, **49A**, 2151 (2018); DOI: 10.1007/s11661-018-4549-8
16. F. Yang, J. Wang, Y. Zhang, et al., *Int. J. Hydrogen Energy*, **47**, 11236 (2022); DOI: 10.1016/j.ijhydene.2022.01.141
17. C. B. Wei, Y. P. Lu, X. H. Du, et al., *Mater. Sci. Eng. A*, **805**, 140548 (2021); DOI: 10.1016/j.msea.2020.140548
18. S. Xiang, H. Luan, J. Wu, et al., *J. Alloy. Compd.*, **773**, 387 (2019); DOI: 10.1016/j.jallcom.2018.09.235
19. A. A. Sayed and S. Kheirandish, *Mater. Sci. Eng. A*, **532**, 21 (2012); DOI: 10.1016/j.msea.2011.10.056
20. Y. Wang, Y. Yuan, J. Yu, et al., *Acta Metall. Sin.*, **57**, 403 (2021); DOI: 10.11900/0412.1961.2020.00494
21. C. H. Tian, D. Ponge, L. Christiansen, and C. Kirchlechner, *Acta Mater.*, **183**, 274 (2020); DOI: 10.1016/j.actamat.2019.11.002
22. L. Huang, Y. Sun, N. Chen, et al., *Mater. Sci. Eng. A*, **830**, 142327 (2022); DOI: 10.1016/j.msea.2021.142327
23. J. B. Seol, D. Raabe, P. P. Choi, et al., *Acta Mater.*, **60**, 6183 (2012); DOI: 10.1016/j.actamat.2012.07.064
24. M. Shabani, J. Indeck, K. Hazeli, et al., *J. Mater. Eng. Perform.*, **28**, 4348 (2019); DOI: 10.1007/s11665-019-04176-y
25. Y. Li, Y. F. Lu, W. Li, et al., *Acta Mater.*, **158**, 79 (2018); DOI: 10.1016/j.actamat.2018.06.019
26. J. Li, W. Jia, J. Wang, et al., *Mater. Des.*, **95**, 183 (2016); DOI: 10.1016/j.matdes.2016.01.112
27. Z. F. He, N. Jia, H. L. Yan, et al., *Int. J. Plast.*, **139**, 102965 (2021); DOI: 10.1016/j.ijplas.2021.102965
28. O. N. Senkov, G. B. Wilks, J. M. Scott, D. B. Miracle, *Intermetallics*, **19**, 698 (2011); DOI: 10.1016/j.intermet.2011.01.004
29. A. Takeuchi and A. Inoue, *Mater. Trans.*, **46**, 2817 (2005); DOI: 10.2320/matertrans.46.2817
30. T. Li, Y. Lu, Z. Cao, et al., *Acta Metall. Sin.*, **57**, 42 (2020); DOI: 10.11900/0412.1961.2020.00293
31. S. J. Lee, Y. S. Jung, S. I. Baik, et al., *Scripta Mater.*, **92**, 23 (2014); DOI: 10.1016/j.scriptamat.2014.08.004
32. L. J. Zhang, Z. K. Jiang, M. D. Zhang, et al., *J. Alloy. Compd.*, **769**, 27 (2018); DOI: 10.1016/j.jallcom.2018.07.329
33. F. Xiong, R. D. Fu, Y. J. Li, et al., *Mater. Sci. Eng. A*, **787**, 139472 (2020); DOI: 10.1016/j.msea.2020.139472
34. X. W. Qiu, Y. P. Zhang, L. He, and C. G. Liu, *J. Alloy. Compd.*, **549**, 195 (2013); DOI: 10.1016/j.jallcom.2012.09.091
35. A. S. Hamdy, E. El-Shenawy, and T. El-Bitar, *Int. J. Electrochem. Sci.*, **1**, 171 (2006); DOI: 10.1016/S1452-3981(23)17147-1
36. N. Kumar, M. Fusco, M. Komarasamy, et al., *J. Nucl. Mater.*, **495**, 154 (2017); DOI: 10.1016/j.jnucmat.2017.08.015
37. Y. Shi, L. Collins, N. Balke, et al., *Appl. Surf. Sci.*, **439**, 533 (2018); DOI: 10.1016/j.apsusc.2018.01.047